Enhanced thermoelectric performance of InTe through Pb doping

Shantanu Misra, Adèle Léon, Petr Levinský, Jiří Hejtmánek, Bertrand Lenoir, Christophe Candolfi

Enhanced thermoelectric performance of InTe through Pb doping

Shantanu Misra[1], Adèle Léon[1], Petr Levinský[2], Jiří Hejtmánek[2], Bertrand Lenoir[1,*], Christophe Candolfi[1,*]

[1] *Institut Jean Lamour, UMR 7198 CNRS – Université de Lorraine, Campus ARTEM, 2 allée André Guinier, BP 50840, 54011 Nancy, France*

[2] *FZU – Institute of Physics of the Czech Academy of Sciences, Cukrovarnická 10/112, 162 00, Prague 6, Czech Republic*

[*]Corresponding authors: christophe.candolfi@univ-lorraine.fr; bertrand.lenoir@univ-lorraine.fr

Abstract

Chalcogenide semiconductors continue to be of prime interest for designing novel efficient materials for energy-conversion applications. Among them, the narrow-band-gap *p*-type semiconductor InTe exhibits high thermoelectric performance that mostly stems from its poor ability to transport heat. Here, we show that its thermoelectric figure of merit can be further enhanced by finely tuning the hole concentration through Pb doping. X-ray diffraction and scanning electron microscopy performed on the polycrystalline series $In_{1-x}Pb_xTe$ confirm that Pb substitutes for In with an estimated solubility limit below 1%. Pb acts as a donor-like impurity, driving the degenerate behavior of pristine InTe towards semiconducting-like properties. The enhanced disorder caused by this substitution increases point-defect scattering of phonons, leading to reduced lattice thermal conductivity. The resulting increase in the power factor and decrease in the phonon transport to values as low as 0.22 W m^{-1} K^{-1} above 700 K

yields a peak *ZT* value of 1.05 at 780 K for $x = 0.1\%$ along the direction parallel to the pressing direction. According to a single parabolic band model, this sample exhibits a near-optimal thermoelectric performance.

1. Introduction

Thermoelectric materials have the ability to convert heat into electrical power and vice versa, providing a versatile technology for power generation and solid-state cooling applications.[1-3] The conversion efficiency of thermoelectric devices is primarily governed by the dimensionless figure of merit *ZT* defined at an absolute temperature *T* as $ZT = \alpha^2 T/\rho\kappa$.[1-4] High efficiency requires to achieve simultaneously a large thermopower (or Seebeck coefficient) α, low electrical resistivity ρ, and low total thermal conductivity κ. Heavily-doped semiconductors with high structural complexity usually possess the most favorable combination of these three mutually-incompatible properties.[1-4] Fulfilling these requirements, chalcogenide semiconductors are a prospective area of research for identifying and designing highly-efficient thermoelectric materials thanks to their chemical robustness that allows for a wide variety of substitutions to be experimentally realized.[5-33] Several strategies have been devised to enhance the power factor α^2/ρ, a list that includes magnetic ion doping[7,8] and band structure engineering tools such as band convergence,[9-11] resonant levels[12-20] or energy-filtering effects.[21,22] Alternatively, another arsenal of techniques has been developed to reduce the lattice thermal conductivity κ_L ($\kappa = \kappa_L + \kappa_e$ with κ_e the electronic contribution) down to its minimum using solid solutions, nanostructuring or the formation of precipitated phases at various length scales.[23-25] Many of these phases show the remarkable ability to poorly conduct heat due to their unusual bonding properties.[5,6] For optimized compositions, higher thermoelectric performance with respect to state-of-the-art thermoelectric materials was achieved, with peak *ZT* values over 1.0 in the 600 – 1000 K temperature range.[5-33]

Among binary chalcogenide semiconductors, InTe stands out due to its very low lattice thermal conductivity of 0.25 W m^{-1} K^{-1} at 800 K, consistently measured in both single-crystalline and polycrystalline samples.[34-44] Inelastic neutron scattering experiments have demonstrated that this remarkable trait is tied to disordered, rattling-like In^{+} cations located in tunnels formed by the infinite linear chains of edge-sharing $(In^{3+}Te_4^{2-})^{-}$ tetrahedra building the tetragonal crystal structure (space group *I*4/*mcm*, No 140).[35] This structural characteristic gives rise to low-energy optical modes that strongly limit the phase space available for acoustic phonons and hence, the ability of the lattice to transport heat. Electronically, pristine InTe behaves as a weakly-degenerate *p*-type semiconductor with an optical band gap on the order of 0.3 eV at 300 K.[34,43] The self-doping is presumably due to a small amount of native In vacancies that shifts the chemical potential near the edge of the valence bands, yielding a finite density of states at the Fermi level.[34] This combination of semiconducting-like electronic properties and reduced lattice thermal conductivity results in high *ZT* values of up to 0.85 at 800 K in polycrystalline samples.[34-37,43]

Given the large number of possible aliovalent substitutions on the In or Te site, alloying is a possible route to further tuning the hole concentration and reducing the lattice thermal conductivity. Here, we investigate the influence of Pb, that maximizes mass and size contrast on the In site, on the high-temperature thermoelectric properties of polycrystalline InTe. Low concentrations of Pb, that acts as a donor impurity, allows for further adjustment of the hole concentration, progressively driving the degenerate properties of InTe towards a semiconducting state. By pushing the intrinsic regime towards higher temperatures, a concentration of Pb as low as 0.1% yields enhanced thermoelectric performance, with a peak *ZT* value of 1.05 at 780 K measured along the direction parallel to the pressing direction.

2. Experimental details

All the handling of the elements and materials was carried out in a dry, Ar-filled glove box. Polycrystalline samples of $In_{1-x}Pb_xTe$ (x = 0.0, 0.10%, 0.25%, 0.50% and 1%) were synthesized by direction reaction of high-purity In (5N+, 99.999%), Te (5N+, 99.999%) and Pb (5N, 99.999%) at high temperatures in sealed silica tubes. Prior to use, the elements were purified to remove any traces of oxides. To this end, In was successively washed in dilute acid and distilled water baths. Te or Pb shots were loaded into degassed silica tubes, sealed under inert atmosphere, and heated above the melting point temperature. The tubes were dwelt for 2 h before being quenched in room-temperature water. Traces of oxides were removed by polishing the surfaces of the resulting ingot, which was subsequently ground into fine powders. The purified In shots and Te and Pb powders were weighed in stoichiometric quantities and loaded into a pre-evacuated silica tube sealed under secondary vacuum. The tubes were placed in a rocking furnace for 15 h at 1023 K before being quenched into room-temperature water. The resulting ingots were hand-crushed into fine powders using an agate mortar. The powders were densified by spark plasma sintering (Dr Sinter 515S SPS Syntex Inc.) at 773 K in a graphite die for 15 min under a uniaxial pressure of 50 MPa. For all samples, the experimental density of the cylindrical pellets, determined from their weight and geometrical dimensions, was found to be higher than 97% of the theoretical density from X-ray diffraction data.[35] Bar-shaped (~8×2×2 mm^3), disc- (ϕ = 10 mm, h = 1.5 mm) and square-shaped (6×6×1.5 mm^3) samples were cut from the consolidated pellets using a diamond-wire saw. Because InTe crystallizes with a tetragonal crystal structure (space group I4/*mcm*), the transport properties are direction dependent in both polycrystalline and single-crystalline compounds.[35,34-37,42,43] For this reason, samples were cut parallel and perpendicular to the SPS pressing direction (Figure S1 in ESI).

The phase purity and crystal structure of the samples were determined at 300 K by powder X-ray diffraction (PXRD) using a Bruker D8 Advance Diffractometer (Cu $K\alpha_1$ radiation). The

chemical composition and homogeneity was investigated by scanning electron microscopy (SEM) and electron dispersive X-ray spectroscopy (EDXS) using a Quanta FEG microscope. Hereafter, the nominal Pb contents will be used to label the samples.

Hall effect measurements were performed on the bar-shaped samples at 300 K with a four-probe configuration using the ETO option of a physical property measurement system (PPMS, Quantum Design). Good electrical contacts were realized by brazing copper wires onto the samples with a tiny amount of low-melting point braze. The Hall resistivity ρ_H was determined by measuring the antisymmetric component of the transverse electrical resistivity ρ_{xy} under magnetic field ($\mu_0 H$) reversal following the formula $\rho_H = \left[\rho_{xy}(+\mu_0 H) - \rho_{xy}(-\mu_0 H)\right]/2$. The Hall coefficient R_H was derived from the slope of the $\rho_H(\mu_0 H)$ data for magnetic fields $-1 \leq \mu_0 H \leq 1$T. The Hall hole concentration p_H and Hall mobility μ_H were determined from the single-carrier relations $p_H = 1/R_H e$ and $\mu_H = R_H/\rho$ where e is the elemental charge. Regardless of the Pb content, no significant anisotropy was observed in the R_H values. Thus, the p_H and μ_H values inferred from the above-mentioned formulas provide reasonable estimates of the actual values.

The thermal diffusivity *a* was measured on the disc-/square-shaped samples between 300 and 800 K using a Netzsch laser flash instrument (LFA 427). Prior to measurements, the samples were spray-coated with a thin layer of graphite to ensure a homogeneous signal absorption and emission on the respective surfaces. The thermal diffusivity was used to calculate the total thermal conductivity κ via the formula $\kappa = aC_p d$ where C_p is the specific heat and d is the experimental density. C_p was approximated by the Dulong-Petit law $C_p = 3NR$ where N is the number of atoms per formula unit and R is the gas constant. The temperature dependence of the density was not taken into account. The thermopower and electric resistivity were measured simultaneously between 300 and 800 K using a ZEM-3 apparatus (Ulvac-Riko) on the bar-shaped samples. The experimental uncertainties in κ, α and

ρ are estimated to be 10, 5 and 5%, respectively, giving rise to an overall uncertainty of 17% in the *ZT* values.[45] Due to the small degree of anisotropy in ρ and α for all samples, the discussion of the transport properties will be based on the measurements performed along the direction parallel to the pressing direction, that is, the direction along which the thermoelectric performance is the highest. Measurements performed along the perpendicular direction are shown in Figures S2 to S6 in the ESI.

3. Results and discussion

The PXRD patterns (Figure 1) for $x < 0.50\%$ can be fully indexed with the tetragonal crystal structure of InTe, with no obvious secondary phases detected. For $x = 0.50$ and 1%, two weak reflections that correspond to the binary PbTe appear, suggesting a low solubility limit of Pb in InTe. SEM images collected in backscattered electron mode and the corresponding elemental X-ray mapping (Figures S7 and S8 in ESI) confirm the absence of secondary phases and the homogeneous spatial distribution of the three elements, except for the $x = 0.50$ and 1% sample for which small Pb-rich areas can be observed. The unit cell volume *V* tends to increase with increasing *x* up to 0.50% (Figure S9 in ESI), in agreement with the larger atomic radius of Pb (175 pm) compared to In (167 pm). The lower value of *V* for $x = 1\%$ compared to that of the $x = 0.50\%$ sample indicates a lower actual Pb content, in agreement with the PXRD and SEM analyses.

The hole concentration p_H decreases by one order of magnitude at 300 K upon increasing the Pb content from 4.5×10^{19} cm^{-3} for $x = 0.0$ to 2.8×10^{18} cm^{-3} for $x = 1\%$, indicating that Pb acts as a donor impurity in InTe. One exception to this general trend is the $x = 0.10\%$ sample that exhibits a slightly higher hole density ($p_H = 6.7\times10^{19}$ cm^{-3}) compared to pristine InTe. The higher p_H of this sample hints to the formation of additional hole-like defects, possibly

promoted by the introduction of Pb. As an alternative scenario, Pb^{2+} might preferentially substitute for In^{3+} cations in the $(In^{3+}Te_4^{2-})^-$ tetrahedra at low doping levels. In contrast, p_H decreases with increasing x for $x \geq 0.25\%$, indicating that Pb^{2+} occupies the site of the In^+ cations in the large tunnels delimited by the infinite chains of edge-sharing tetrahedra running along the c axis. For all samples, the Hall mobility μ_H remains very low (varying between 8 and 17 $cm^2\ V^{-1}\ s^{-1}$ at 300 K for x = 0.1% and 1%, respectively), possibly due to strong charge carrier scattering induced by the disordered In^+ cations. μ_H slightly increases with x due to the decrease in p_H, which probably counterbalances the decrease expected from the enhanced atomic disorder caused by Pb alloying.

In agreement with a decreasing hole density, both the electrical resistivity ρ and thermopower α increase with x (Figures 2a and 2b). This trend suggests that the small concentration of In vacancies that gives rise to metallic-like electronic properties in polycrystalline and single-crystalline InTe is suppressed for $x > 0.10\%$, leading to lightly-doped semiconducting properties. Of note, the anisotropy observed between the basal plane (ab) and the c axis in both ρ and α in single-crystalline InTe is reduced,[34] albeit still present in the Pb-doped samples (see Figures S1 and S2 in ESI). From the maximum α value of the x = 1% sample ($\alpha_{max} = 380\ \mu V\ K^{-1}$) and the corresponding temperature ($T_{max} = 470$ K), the thermal band gap E_g was estimated using the Goldsmid-Sharp relation $E_g = 2e\alpha_{max}T_{max}$ to be 0.35 eV, which is in reasonable agreement with that estimated by absorption spectroscopy on Cd-doped polycrystalline samples (0.22 eV) and from transport data on single-crystalline InTe (0.26 eV).[34,43] The hole concentration dependence of α closely follows the Ioffe-Pisarenko plot calculated from transport data measured on single-crystalline InTe (Figure 3).[34,46] The fact that the density-of-states effective mass m^*_{DOS} only weakly varies with x further indicates that Pb can be considered to behave as a rigid-like impurity in InTe.

The nearly equivalent ρ and α values measured in the $x = 0.0$ and 0.1% Pb-doped samples lead to similar maximum power factors α^2/ρ (Figure 4) with the notable difference of the temperature at which these maxima occur. Compared to pristine InTe, substituting with Pb shifts the maximum towards higher temperatures with a maximum achieved at 700 K. Upon further increasing the Pb content, the power factor is significantly reduced due to the high ρ values that characterize these samples.

The temperature dependence of the total thermal conductivity κ is shown in Figure 5a. For all samples, the κ values are very low over the entire temperature range, ranging at 300 K between 0.82 W m^{-1} K^{-1} for pristine InTe and 0.45 W m^{-1} K^{-1} for the $x = 1.0\%$ sample. Unlike the electronic properties that show a weak degree of anisotropy, the κ values are anisotropic, with the values measured in the parallel direction being systematically lower than those measured in the perpendicular direction (see Figure S5 in ESI). The ratio $\kappa_{\parallel}/\kappa_{\perp}$ is nearly independent of the Pb content and only weakly varies upon heating. For $x \geq 0.25\%$, the upturn in $\kappa(T)$ observed above 550 K is due to the thermal activation of minority carriers across the band gap that leads to an additional bipolar contribution. Based on the Wiedemann-Franz law $\kappa_e = LT/\rho$, where L is the Lorenz number, the high ρ values of the Pb-doped samples for $x \geq$ 0.25% yield negligible electronic contributions κ_e, making the assumption $\kappa \approx \kappa_L$ adequate in the present case. For the x = 0.0 and 0.1% samples, the temperature dependence of L was estimated using a single parabolic band model with acoustic phonon scattering as the dominant source of hole diffusion (Figure S10 in ESI).[46] At 300 K, κ_L decreases with increasing x from 0.75 W m^{-1} K^{-1} for x = 0.0 to 0.42 W m^{-1} K^{-1} for x = 1% (Figure 5b). The decreasing κ_L is consistent with enhanced point-defect scattering expected upon increasing disorder in the unit cell. The relation between the lattice thermal conductivity of the alloyed samples and that of pristine InTe proposed by Klemens and Callaway (Refs. 47-49, see ESI for equations) qualitatively accounts for the observed decrease in κ_L at 300 K indicating that mass contrast

contributes to lower κ_L. Interestingly, the reduction in κ_L induced by doping levels as low as 0.25% and 0.5% seems larger than those expected solely by mass contrast (Figure S11 in ESI), possibly signaling an additional source of phonon diffusion. One possibility to explain this behavior could be the insertion of Pb on the In^{3+} site or on an interstitial site at low doping levels. The latter mechanism has been shown to yield significantly lower κ_L values than expected from conventional point-defect scattering in Cu-doped Mg_3Sb_2 and Zn_4Sb_3.[50-52] This possibility will require further synchrotron/neutron diffraction experiments to determine the position of Pb in the crystal structure as a function of *x* and its possible disordered character if located in the tunnels. Upon heating, κ_L further decreases for the *x* = 0.0 and 0.1% samples to reach extremely low values of 0.28 and 0.22 W m^{-1} K^{-1}, respectively, at 773 K. Regardless of the Pb content, κ_L reaches the amorphous limit $\kappa_{glass} \approx 0.33$ W m^{-1} K^{-1} at high temperatures, estimated using the model developed by Cahill and Pohl.[53] Similar to what has been observed in single-crystalline InTe,[34] the κ_L values of the *x* = 0.0, 0.1 and 0.25% drop below this limit, suggesting that the minimum lattice thermal conductivity might be set by the diffusive limit $\kappa_{diff} \approx 0.21$ W m^{-1} K^{-1} at high temperatures.[54,55]

The temperature dependence of the dimensionless thermoelectric figure of merit *ZT* is shown in Figure 6a. For all samples, the *ZT* values are anisotropic (see Figure S6 in ESI) due to the anisotropy in the thermal transport, which is only partially counterbalanced by the reversed anisotropy observed in the electronic properties. The maximum *ZT* increases from 0.82 for pristine InTe to 1.05 at 790 K for *x* = 0.1% in the direction parallel to the pressing direction, which is the highest value achieved so far for InTe-doped samples (Figure 6b). Measurements performed on a second sample indicate good reproducibility to within experimental uncertainty (Figure S12 in ESI). The *ZT* values decrease significantly for higher Pb concentrations due to the significant increase in the ρ values. The analysis of the hole dependence of *ZT* carried out using the SPB model (see ESI for equations) at 750 K (Figure 6c) indicates that the peak value

achieved for x = 0.1% is very close to the predicted optimum value, leaving little-to-no room for further optimization using donor-like, rigid-like impurities.

4. Conclusion

In summary, the influence of Pb doping on the thermoelectric properties of the chalcogenide semiconductor InTe was studied between 300 and 800 K. PXRD and SEM analyses indicate that the solubility limit of Pb in InTe is below 1%. Electronic transport measurements show that the hole concentration tends to decrease with increasing the Pb content, giving rise to semiconducting-like properties characterized by high electrical resistivity and thermopower values. The increased atomic disorder caused by alloying results in a further reduction in lattice thermal conductivity at room temperature, which can be qualitatively accounted for by classical models of alloy scattering. This doping effect yields a maximum ZT value of 1.05 at 800 K for x = 0.1%, which represents a 25% increase with respect to that achieved in pristine InTe. Because this peak ZT value is close to the optimum value predicted by a single-parabolic band model, further optimization might be achieved by substituting with non-rigid-band-like impurities or by probing deeper into the valence bands where non-parabolic-band effects might emerge, meanwhile maintaining the samples degenerate to higher temperatures.

Acknowledgements

P. L. and J. H. acknowledge the financial support of the Czech Science Foundation (project 18-12761S). Experiments were performed in MGML (mgml.eu), which is supported within the program of Czech Research Infrastructures (project no. LM2018096).

References

[1] D. M. Rowe, *Thermoelectrics and its Energy Harvesting*, CRC Press, Boca Raton, FL, 2012.

[2] H. J. Goldsmid, *Thermoelectric Refrigeration*. Springer, New York, USA, 1964.

[3] L. E. Bell, *Science*, 2008, **321**, 1457–1461.

[4] I. Petsagkourakis, K. Tybrandt, X. Crispin, I. Ohkubo, N. Satoh and T. Mori, *Sci. Tech. Adv. Mater.*, 2018, **19**, 836–862.

[5] Y. Yu, M. Cagnoni, O. Cojocaru-Mirédin and M. Wuttig, *Adv. Funct. Mater*., 2020, **30**, 1904862.

[6] R. Woods-Robinson, Y. Han, H. Zhang, T. Ablekim, I. Khan, K. A. Persson and A. Kutayev, *Chem. Rev*., 2020, **120**, 4007–4055.

[7] J.-B. Vaney, S. Aminorroaya Yamini, H. Takaki, K. Kobayashi, N. Kobayashi and T. Mori, *Mater. Today Phys.*, 2019, **9**, 100090.

[8] N. Tsujii, A. Nishide, J. Hayakawa and T. Mori, *Sci. Adv.*, 2019, **5**, eaat5935.

[9] J. Zhang, R. Liu, N. Cheng, Y. Zhang, J. Yang, C. Uher, X. Shi, L. Chen and W. Zhang, *Adv. Mater*., 2014, **26**, 3848–3853.

[10] Y. Pei, X. Shi, A. LaLonde, H. Wang, L. Chen and G. J. Snyder, *Nature*, 2011, **473**, 66–69.

[11] K. H. Lee, S. Kim, H. S. Kim and S. W. Kim, *ACS Appl. Energy Mater*., 2020, **3**, 2214–2223.

[12] C M. Jaworski, V. Kulbachinskii and J. P. Heremans, *Phys. Rev. B*, 2009, **80**, 233201.

[13] J. P. Heremans, V. Jovovic, E. S. Toberer, A. Saramat, K. Kurosaki, A. Charoenphakdee, S. Yamanaka and G. J. Snyder, *Science*, 2008, **321**, 554–557.

[14] J. P. Heremans, B. Wiendlocha and A.M. Chamoire, *Energy Environ. Sci*., 2012, **5**, 5510–5530.

[15] S. Misra, B. Wiendlocha, J. Tobola, F. Fesquet, A. Dauscher, B. Lenoir and C. Candolfi, *J. Mater. Chem. C*, 2020, **8**, 977–988.

[16] B. Wiendlocha, J. B. Vaney, C. Candolfi, A. Dauscher, B. Lenoir and J. Tobola, *Phys. Chem. Chem. Phys*., 2018, **20**, 12948–12957.

[17] K. T. Wojciechowski, T. Parashchuk, B. Wiendlocha, O. Cherniushok and Z. Dashevsky, *J. Mater. Chem. C*, 2020, **8**, 13270–13285.

[18] M. Kriener, M. Sakano, M. Kamitani, M. S. Bahramy, R. Yukawa, K. Horiba, H. Kumigashira, K. Ishizaka, Y. Tokura and Y. Taguchi, *Phys. Rev. Lett*., 2020, **124**, 047002.

[19] B. Wiendlocha, S. Misra, A. Dauscher, B. Lenoir and C. Candolfi, *Mater*. *Horiz.*, 2021, **8**, 1735–1743.

[20] Q. Zhang, H. Wang, W. Liu, H. Wang, B. Yu, Q. Zhang, Z. Tian, G. Ni, S. Lee, K. Esfarjani, G. Chen and Z. Ren, *Energy Environ. Sci*., 2012, **5**, 5246–5251.

[21] D. Narducci, E. Selezneva, G. Cerofolini, S. Frabboni and G. Ottaviani, *J. Solid State Chem.*, 2012, **193**, 19–25.

[22] C. Gayner and Y. Amouyal, *Adv. Funct. Mater.*, 2019, **30**, 1901789.

[23] L. You, Y. Liu, X. Li, P. Nan, B. Ge, Y. Jiang, P. Luo, S. Pan, Y. Pei, W. Zhang, G. J. Snyder, J. Yang, Y. Zhang and J. Luo, *Energy Environ. Sci.*, **2018**, 11, 1848–1858.

[24] Y. Pei, J. Lensch-Falk, E. S. Toberer, D. L. Medlin and G. J. Snyder, *Adv. Funct. Mater.*, 2011, **21**, 241–249.

[25] Y. Pei, N. A. Heinz, A. LaLonde and G. J. Snyder, *Energy Environ. Sci.*, 2011, **4**, 3640–3645.

[26] W. Zhang, N. Sato, K. Tobita, K. Kimura and T. Mori, *Chem. Mater.*, 2020, **32**, 5335–5342.

[27] J. Shen, Z. Chen, S. Lin, L. Zheng, W. Li and Y. Pei, *J. Mater. Chem. C*, 2016, **4**, 209–214.

[28] G. Guélou, P. Lemoine, B. Raveau and E. Guilmeau, *J. Mater. Chem. C*, 2021, **9**, 773–795.

[29] P. Kumar-Ventrapati, S. Misra, G. Delaizir, A. Dauscher, B. Lenoir and C. Candolfi, *J. Mater. Chem. C*, 2020, **8**, 14037–14048.

[30] D. Souchay, M. Nentwig, D. Günther, S. Keilholz, J. de Boor, A. Zeugner, A. Isaeva, M. Ruck, A. U. B. Wolter, B. Büchner and O. Oeckler, *J. Mater. Chem. C*, 2019, **7**, 9939–9953.

[31] Y. Gan, Y. Huang, N. Miao, J. Zhou and Z. Sun, *J. Mater. Chem. C*, 2021, **9**, 4189–4199.

[32] N. Jia, J. Cao, X. Y. Tan, J. Zhang, S. W. Chien, L. Yang, K. Chen, H. K. Ng, S. S. F. Duran, H. Liu, C. K. I. Tan, Z. Li, J. Xu, J. Wu, Q. Yan and A. Suwardi, *J. Mater. Chem. A*, 2021, doi.org/10.1039/D1TA05866E.

[33] Y. Zheng, T. J. Slade, L. Hu, X. Y. Tan, Y. Luo, Z.-Z. Luo, J. Xu, Q. Yan and M. G. Kanatzidis, *Chem. Soc. Rev.*, 2021, **50**, 9022–9054.

[34] S. Misra, Petr Levinský, A. Dauscher, G. Medjahdi, J. Hejtmánek, B. Malaman, G. J. Snyder, B. Lenoir and C. Candolfi, *J. Mater. Chem. C*, 2021, **9**, 5250–5260.

[35] T. Chattopadhyay, R. P. Santandrea and H. G. von Schnering, *J. Phys. Chem. Solids*, 1985, **46**, 351–356.

[36] M. K. Jana, K. Pal, U. V. Waghmare and K. Biswas, *Angew. Chem*., 2016, **55**, 7792–7796.

[37] S. Y. Back, H. Cho, Y. K. Kim, S. Byeon, H. Jin, K. Koumoto and J. S. Rhyee, *AIP Adv*., 2018, **8**, 115227.

[38] H. Zhu, B. Zhang, G. Wang, K. Peng, Y. Yan, Q. Zhang, X. Han, G. Wang, X. Lu and X. Zhou, *J. Mater. Chem. A*, 2019, **7**, 11690–11698.

[39] S. Y. Back, Y. K. Kim, H. Cho, M. K. Han, S. J. Kim and J. S. Rhyee, *ACS Appl. Energy Mater*., 2020, **3**, 3628–3636.

[40] S. Pal and D. N. Bose, *Solid State Commun*., 1996, **97**, 725–729.

[41] M. A. Nizametdinova, *Phys. Stat. Sol. (b),* 1980, **97**, K9–K12.

[42] V. Rajaji, K. Pal, S. Ch. Sarma, B. Joseph, S. C. Peter, U. V. Waghmare, C. Narayana, *Phys. Rev. B*, 2018, **97**, 155158.

[43] S. Pan, H. Liu, Z. Li, L. You, S. Dai, J. Yang, K. Guo and J. Luo, *J. Alloy Compd.,* 2020, **813**, 152210.

[44] S. Misra, C. Barreteau, J. C. Crivello, V. M. Giordano, J. Castellan, Y. Sidis, P. Levinský, J. Hejtmánek, B. Malaman, A. Dauscher, B. Lenoir, C. Candolfi and S. Pailhès, *Phys. Rev. Research*, 2020, **2**, 043371.

[45] E. Alleno, D. Bérardan, C. Byl, C. Candolfi, R. Daou, R. Decourt, E. Guilmeau, S. Hébert, J. Hejtmanek, B. Lenoir, P. Masschelein, V. Ohorodniichuk, M. Pollet, S. Populoh, D. Ravot, O. Rouleau and A. M. Soulier, *Rev. Sci. Instrum*., 2015, **86**, 011301.

[46] V. I. Fistul, *Heavily Doped Semiconductors*, Plenum Press, New York, 1969.

[47] B. Abeles, *Phys. Rev.*, 1963, **131**, 1906–1911.

[48] *P. G. Klemens*, Phys. Rev., 1960, **119**, 507–509.

[49] J. Callaway and H. C. von Baeyer, *Phys. Rev.*, 1960, **120**, 1149–1154.

[50] Z. Liu, N. Sato, W. Gao, K. Yubuta, N. Kawamoto, M. Mitome, K. Kurashima, Y. Owada, K. Nagase, C.-H. Lee, J. Yi, K. Tsuchiya and T. Mori, *Joule*, 2021, **5**, 1196–1208.

[51] G. J. Snyder, M. Christensen, E. Nishibori, T. Caillat and B. B. Iversen, *Nat. Mater.*, 2004, **3**, 458–463.

[52] F. Cargnoni, E. Nishibori, P. Rabiller, L. Bertini, G. J. Snyder, M. Christensen, C. Gatti, and B. B. Iversen, *Chem. Eur. J.*, 2004, **10**, 3861–3870.

[53] D. G. Cahill, S. K. Watson and R. O. Pohl, *Phys. Rev. B*. 1992, **46**, 6131–6140.

[54] A. F. Ioffe and A. R. Regel, *Prog. Semicond*., 1960, **4**, 237–291.

[55] M. T. Agne, R. Hanus and G. J. Snyder, *Energy Environ. Sci*., 2018, **11**, 609–616.

Figure captions

Fig. 1 PXRD patterns for the x = 0.0, 0.10, 0.25, 0.50 and 1% Pb-doped samples. For the x = 0.5% and 1% sample, the asterisks indicate the secondary phases identified as PbTe. The variations in the relative intensities of the main diffraction peaks from sample to sample is due to the anisotropic crystal structure of InTe that leads to some preferred orientation of the crystallites.

Fig. 2 Temperature dependence of a) electrical resistivity ρ and b) thermopower α measured in the direction parallel to the pressing direction for the x = 0.0, 0.10, 0.25, 0.50 and 1% Pb-doped samples.

Fig. 3 Ioffe-Pisarenko plot showing the hole concentration dependence of the thermopower $\alpha(p)$. The solid and dashed curves show the theoretical dependence calculated by the SPB model. Data obtained on single-crystalline (SC) InTe along the *c* axis and the basal (*ab*) plane (Ref. 34), on polycrystalline pristine InTe in prior studies (Refs. 36, 37 and 40) and on polycrystalline Cd-doped samples (Ref. 43) have been added.

Fig. 4 Temperature dependence of the power factor α^2/ρ along the direction parallel to the pressing direction for the x = 0.0, 0.10, 0.25, 0.50 and 1% Pb-doped samples.

Fig. 5 Temperature dependence of the a) total thermal conductivity κ and b) lattice thermal conductivity κ_L measured in the direction parallel to the pressing direction for the x = 0.0, 0.10, 0.25, 0.50 and 1% Pb-doped samples. In panel b), the two horizontal dashed lines stand for the glassy and diffusive lower bounds of κ_L calculated using the experimental sound velocities measured on single-crystalline InTe (Ref. 34).

Fig. 6 a) Temperature dependence of the dimensionless thermoelectric figure of merit *ZT* along the direction parallel to the pressing direction for the x = 0.0, 0.1, 0.25, 0.5 and 1% Pb-doped samples. b) Comparison of the *ZT* values measured for the optimized Pb-doped sample x = 0.1% with those reported in the literature on polycrystalline InTe (Ref. 37), In-deficient InTe (Ref. 36) and Sb- (Ref. 38) and Cd-doped (Ref. 43) InTe samples. c) Hole dependence of the experimental *ZT* values for the x = 0.0, 0.1, 0.25, 0.5 and 1% Pb-doped samples. The solid and dashed curves were calculated at 750 K for InTe and Pb-doped samples using a single parabolic band model (see ESI for the equations and values of the physical parameters used).

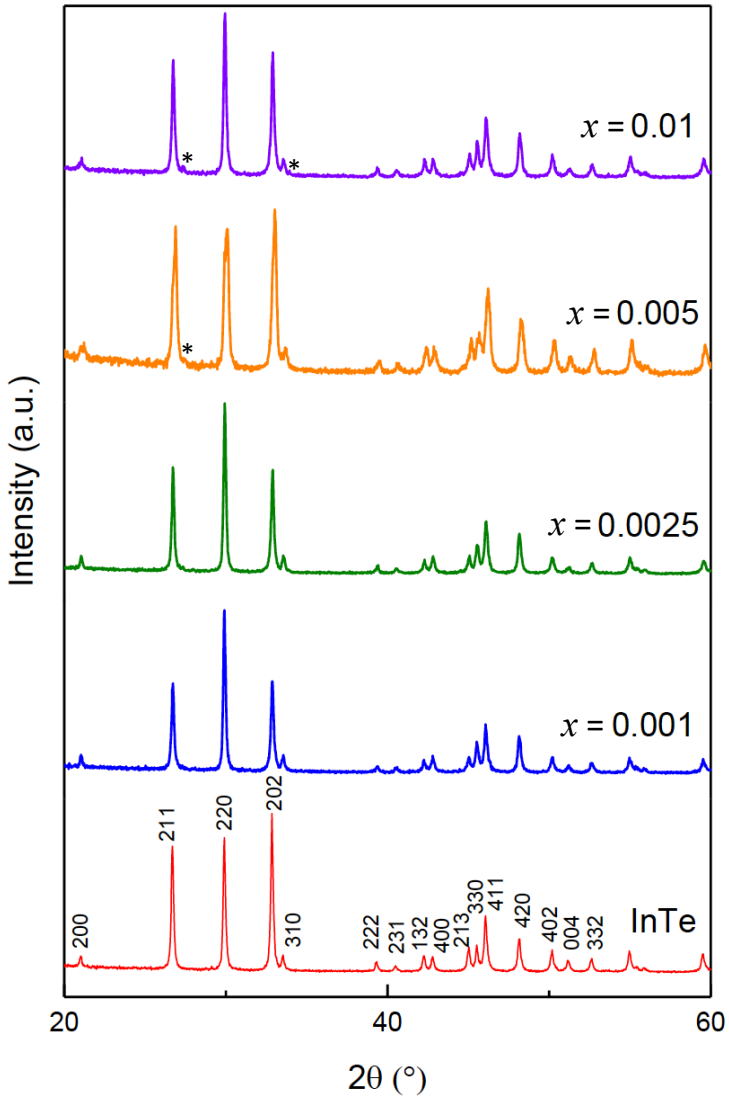
x = 0.01
x = 0.005
x = 0.0025
x = 0.001
InTe
Intensity (a.u.)
2θ (°)
20
40
60
200
211
220
202
310
222
231
132
400
213
330
411
420
402
004
332

Figure 1

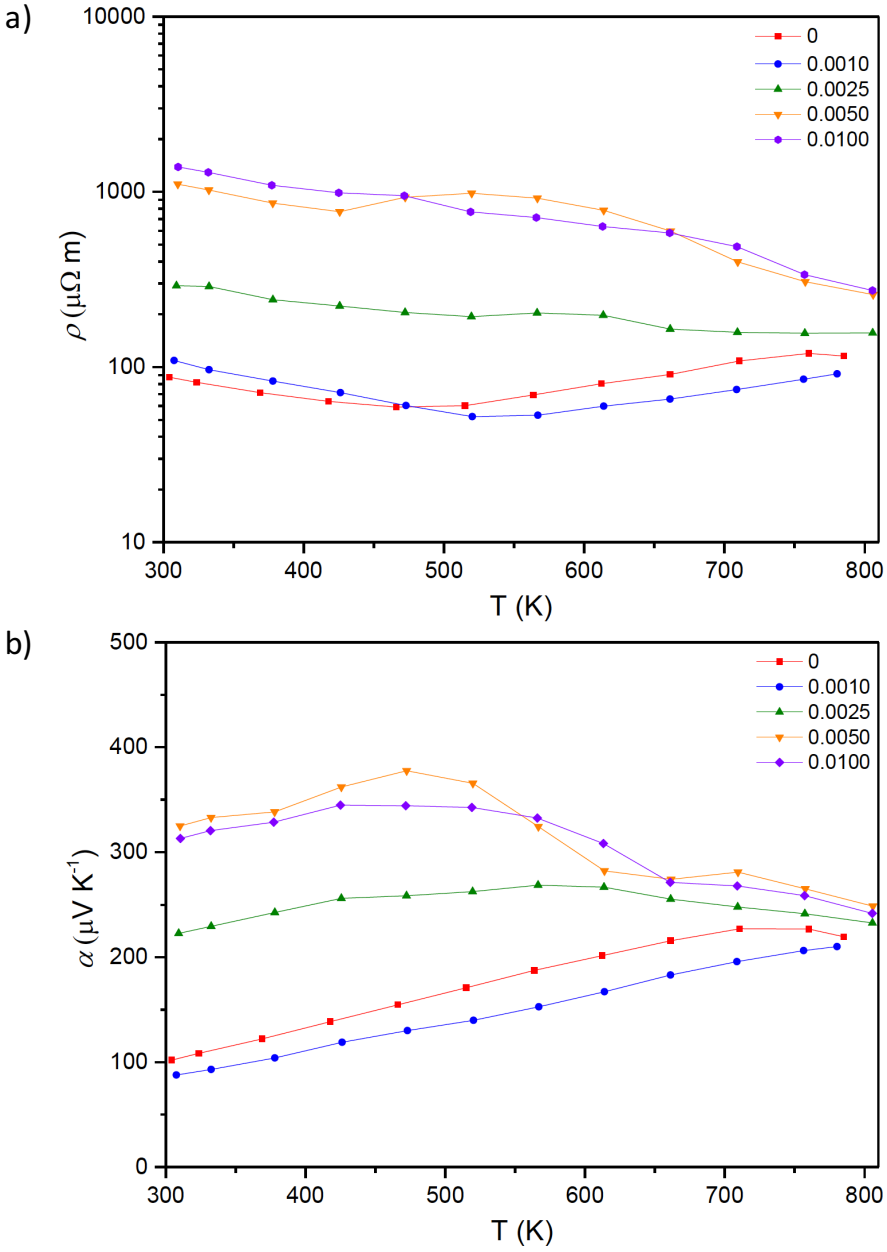
a)
10000
1000
100
10
ρ (μΩ m)
300
400
500
600
700
800
T (K)
0
0.0010
0.0025
0.0050
0.0100
b)
500
400
300
200
100
0
α (μV K⁻¹)
300
400
500
600
700
800
T (K)
0
0.0010
0.0025
0.0050
0.0100

Figure 2

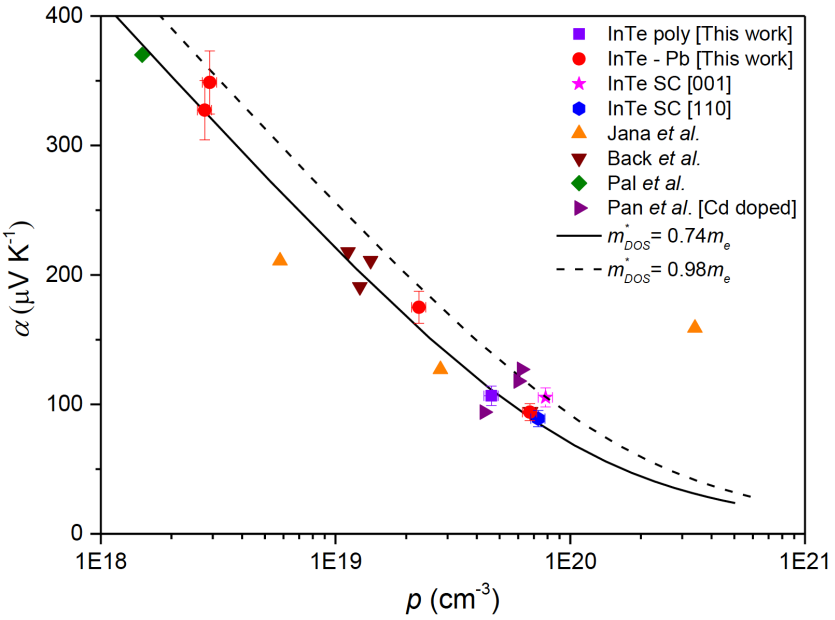
400
300
200
100
0
1E18
1E19
1E20
1E21
α (μV K-1)
p (cm-3)
InTe poly [This work]
InTe - Pb [This work]
InTe SC [001]
InTe SC [110]
Jana et al.
Back et al.
Pal et al.
Pan et al. [Cd doped]
m*DOS= 0.74me
m*DOS= 0.98me

Figure 3

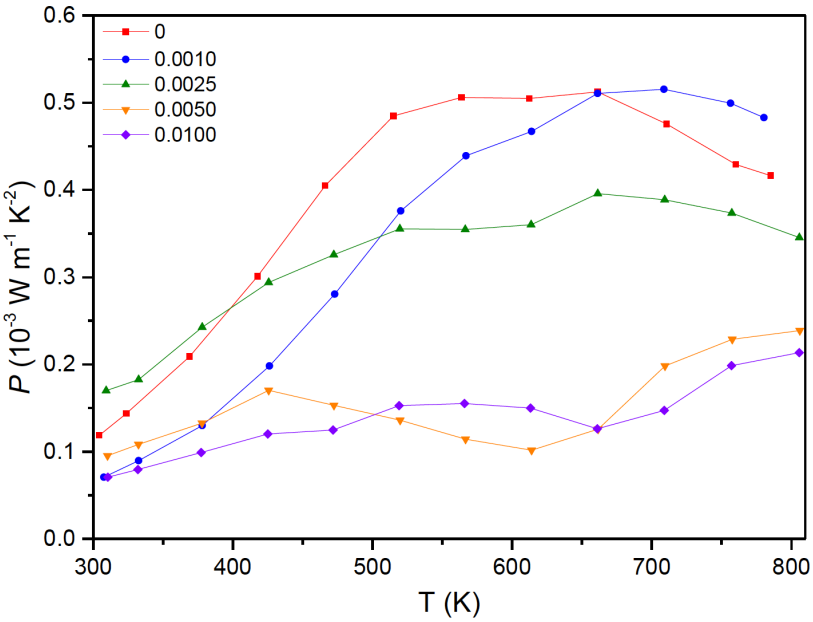
0
0.0010
0.0025
0.0050
0.0100
P (10-3 W m-1 K-2)
T (K)
0.0
0.1
0.2
0.3
0.4
0.5
0.6
300
400
500
600
700
800

Figure 4

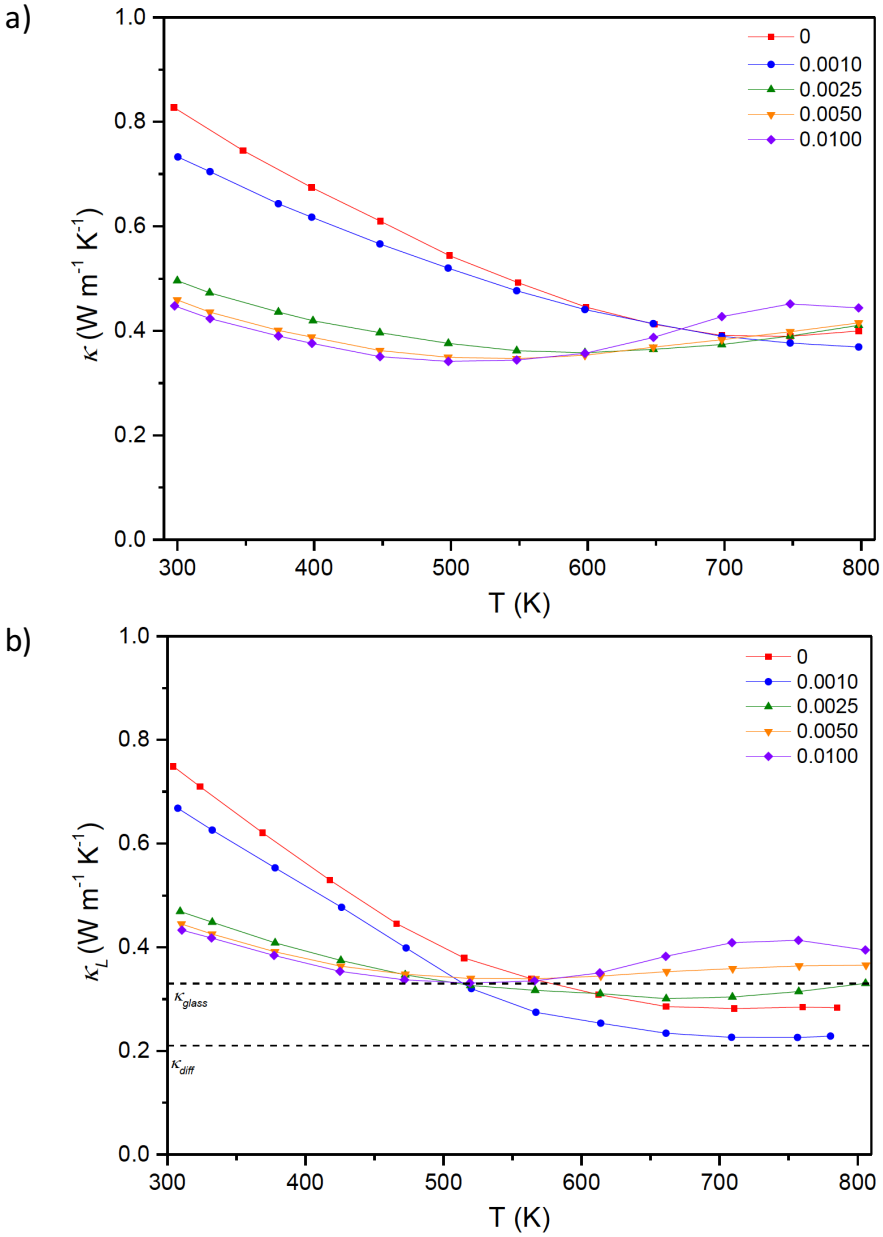
a)
1.0
0.8
0.6
0.4
0.2
0.0
κ (W m-1 K-1)
300
400
500
600
700
800
T (K)
0
0.0010
0.0025
0.0050
0.0100
b)
1.0
0.8
0.6
0.4
0.2
0.0
κL (W m-1 K-1)
κglass
κdiff
300
400
500
600
700
800
T (K)
0
0.0010
0.0025
0.0050
0.0100

Figure 5

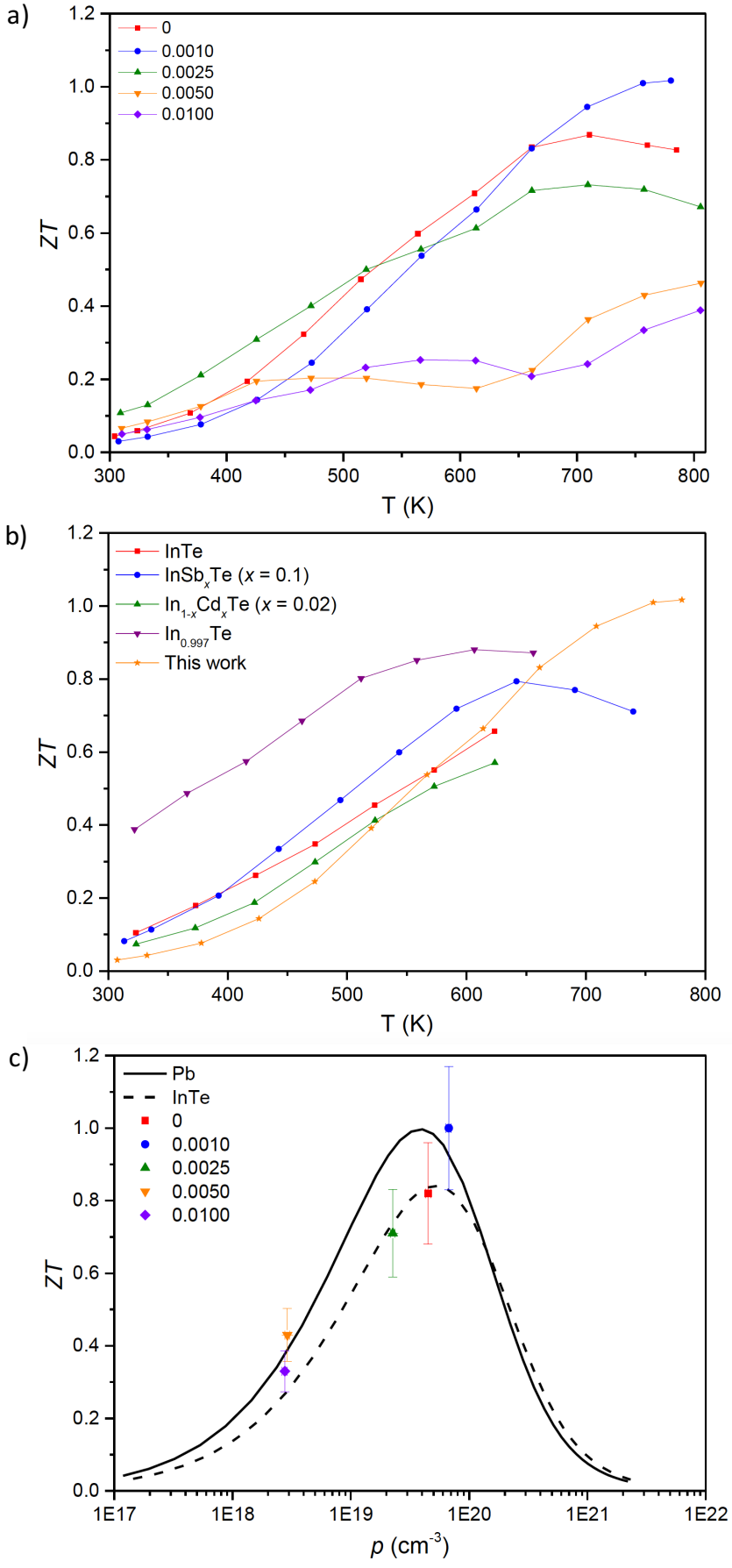
a)
0
0.0010
0.0025
0.0050
0.0100
ZT
T (K)
b)
InTe
InSb$_x$Te (x = 0.1)
In$_{1-x}$Cd$_x$Te (x = 0.02)
In$_{0.997}$Te
This work
ZT
T (K)
c)
Pb
InTe
0
0.0010
0.0025
0.0050
0.0100
ZT
p (cm^{-3})

Figure 6